metals

MDPI

Article

An Effective Strengthening Strategy of Nano Carbide Precipitation and Cellular Microstructure Refinement in a Superalloy Fabricated by Selective Laser Melting Process

Kai-Chun Chang [1], Meng-Yun Lee [1,2], Tzu-Hou Hsu [1], Yao-Jen Chang [1,3], Kai-Chi Lo [1,3], Hyoung Seop Kim [2], Kuo-Kuang Jen [4] and An-Chou Yeh [1,3,*]

1 Department of Materials Science and Engineering, National Tsing Hua University, 101, Sec. 2, Kuang-Fu Road, Hsinchu 30013, Taiwan; stes9151203@yahoo.com.tw (K.-C.C.); mengyun86417@gapp.nthu.edu.tw (M.-Y.L.); cykf.billy@gmail.com (T.-H.H.); Changyj@mx.nthu.edu.tw (Y.-J.C.); kaichi.lo@mx.nthu.edu.tw (K.-C.L.)
2 Department of Materials Science and Engineering, Pohang University of Science and Technology (POSTECH), Pohang 37673, Korea; hskim@postech.ac.kr
3 High Entropy Materials Center, National Tsing Hua University, 101, Sec. 2, Kuang-Fu Road, Hsinchu 30013, Taiwan
4 Missile and Rocket System Research Division, National Chung-Shan Institute of Science and Technology, Taoyuan 325, Taiwan; rgg@ms7.hinet.net
* Correspondence: yehac@mx.nthu.edu.tw

Abstract: An effective strategy to strengthen a superalloy processed by selective laser melting (SLM) is proposed. The aim is to increase the yield strength of Inconel 718 fabricated by SLM to beyond 1400 MPa, which has never been achieved before. In this study, various NbC additions (0.0%, 0.5%, 1.0%, and 5.0% by weight) were added in the powder bed of Inconel 718, and two types of post-SLM heat treatments were investigated, i.e., solution heat treated plus aging (STA) and direct aging (DA). With NbC addition, smaller depth of melt pool and finer dendritic cells were obtained. Both STA and DA promoted the precipitations of γ' and γ''. STA eliminated the cellular dendrites and induced grain growth while DA retained the as-built cellular dendrites, grain size, and nano-carbide from NbC addition, rendering a significant 326.2 MPa increase in yield strength. In this work, 0.5% NbC addition exhibited a record-high yield strength of 1461 MPa and ultimate tensile strength of 1575 MPa for Inconel 718 processed by laser manufacturing process according to literature data to-date.

Keywords: selective laser melting; superalloy; cellular structure; tensile properties

check for updates

Citation: Chang, K.-C.; Lee, M.-Y.; Hsu, T.-H.; Chang, Y.-J.; Lo, K.-C.; Kim, H.S.; Jen, K.-K.; Yeh, A.-C. An Effective Strengthening Strategy of Nano Carbide Precipitation and Cellular Microstructure Refinement in a Superalloy Fabricated by Selective Laser Melting Process. *Metals* **2021**, *11*, 1691. https://doi.org/10.3390/met11111691

Academic Editors: Thomas Niendorf and Jose Eduardo Spinelli

Received: 23 September 2021
Accepted: 19 October 2021
Published: 23 October 2021

1. Introduction

Inconel 718 superalloy is a high strength structural material widely used in oil-gas industry [1,2]. It is primarily precipitation strengthened by coherent $L1_2$ structured γ' (Ni_3 (Al, Ti)) phase and DO_{22} structured γ'' (Ni_3Nb) phase [3]. Engineering components used in oil-gas industries such as drills for deep-water operation are made of Inconel 718 and it is required to possess a yield strength beyond 1400 MPa at ambient temperature [2,4], but the standard heat treated Inconel 718 could possess only a yield strength of 900~1200 MPa [5,6]; to meet such ultra-high strength demand, additional strengthening contributions from grain refinement [7] and strain hardening [8,9] have been applied in addition to precipitation strengthening [8]. However, conventional wrought processes for Inconel 718 could limit the design complexity of the component and lead to waste of material during machining processes, recently the fused-based additive manufacturing (AM) for Inconel 718 has been a subject of interest [5,6,10–24]. During the AM process, powder feedstocks are fused layer by layer to build components with complex geometry without modules. Among various fused-based AM technologies, powder bed selective laser melting (SLM) possesses the ability to make intricate parts with high cost-efficiency [25–27]; it permits part design with more complex geometries and better quality of surface finish compared to those made by

powder jetted laser engineered net shaping (LENS) [25,26]. On the other hand, the SLM process does not require a working chamber under vacuum, which is required by powder bed Electron Beam Melting process [24]. Hence, SLM is considered as one of the main AM processes for Inconel 718 [5,6,10–19], and it is of interest to the oil-gas industries to explore the possibility to fabricate ultra high strength Inconel 718 by SLM process [28]. It has been reported that residual strain induced by thermal contraction during the SLM fusion process could provide an extra strength of about 268 MPa on average [29–31]. For SLM Inconel 718, Kuo et al. [18] reported that residual strain from SLM process could be retained by direct aging process, and dislocation and sub-grains strengthening could render a yield strength of 1380 MPa; a similar result was reported by Deng et al. [11]: tensile yield strength of 1350 MPa was achieved by direct aging after SLM. To date, the highest reported tensile strength for Inconel 718 processed by SLM was 1365 MPa on average, which was still lower than that demanded by the oil-gas industry.

In principle, a further increase in thermally induced strain by SLM for strengthening could be achieved through adjusting scanning parameters [32–34]. However, this approach could also result in distortion or cracking of the built [32–34]. Alternatively, the introduction of inclusions could provide further strengthening for SLM metal alloys [16,29–31,35]. In the work of Kim et al. [29], Mn-based oxide formed in CoCrFeMnNi during SLM process could strengthen the material and result in yield strength of 778.4 MPa. A similar observation was reported by Lin et al. [30]; Al/Ti-based oxide formed in SLM $Al_{0.2}Co_{1.5}CrFeNi_{1.5}Ti_{0.3}$ alloy could further increase the strength by 170 MPa. Moreover, in our previous work [16], 0.2 wt% $CoAl_2O_4$ was added to fabricate Inconel 718 by SLM process followed by solution and aging treatment; this approach resulted in the formation of Al-rich oxide and rendered a yield strength of 1161 MPa. Almangour et al. [31] reported that TiB2 addition not only provided an Orowan strengthening of 268 MPa in average to SLM 316L stainless steel, cellular structure with composition segregation was also refined and contributed an extra 61 MPa in average to yield stress; Han et al. [35] also reported an increase of 100 MPa in tensile strength for SLM Hatstelloy X with TiC addition.

According to literature to-date for laser manufactured Inconel 718, none has achieved a tensile yield strength greater than 1400 MPa. However, two separate approaches have shown great potentials to provide further strengthening contributions: one is by post-SLM direct aging [11,18] and the other is by adding inclusions prior to SLM [16,29–31,35]. To the best of the authors' knowledge, no one has attempted to combine both approaches to enhance the strength of SLM Inconel 718. In this study, the objective is to fabricate high-strength Inconel 718 by SLM, with the aim to achieve yield strength greater than 1400 MPa. NbC was chosen as the inclusion since the elementary constituents of NbC are that of Inconel 718. The influence of NbC on the microstructure of SLM Inconel 718 has been examined; strengthening contributions with direct aging have been elucidated and discussed. This work presents an effective strategy to fabricate Inconel 718 by SLM with yield strength greater than 1400 MPa.

2. Materials and Methods

2.1. Powder Materials Preparation

Gas atomize powder of Inconel 718 was supplied by Chung Yo materials Co., Ltd. Kaohsiung City, Taiwan. The composition of the powder was analyzed by ICP-OES/carbon analyzer, and is presented in Table 1. The d_{50} of the powder was 32.84 μm, which was determined by a laser diffraction particle size analyzer (Coulter LS230, Beckman Coulter Inc., Brea, CA, USA). The inclusion was NbC flakes provided by Ultimate material technology Co., Ltd., Taiwan; d_{50} of NbC powder was 2.239 μm. In this work, various amounts of NbC flakes (0.5%, 1.0%, and 5.0% in weight) were blended with Inconel 718 powder by 2D powder mixing process for 1 h to ensure homogeneity. Figures 1 and 2 shows the morphology and the size distribution of the Inconel 718 powders and NbC flakes used in this study.

Table 1. Inconel 718 powder composition in this work.

Element	Ni	Cr	Fe	Nb	Mo	Al	Ti	C
at%	51.00	19.63	21.51	3.39	1.85	1.23	1.26	0.1334

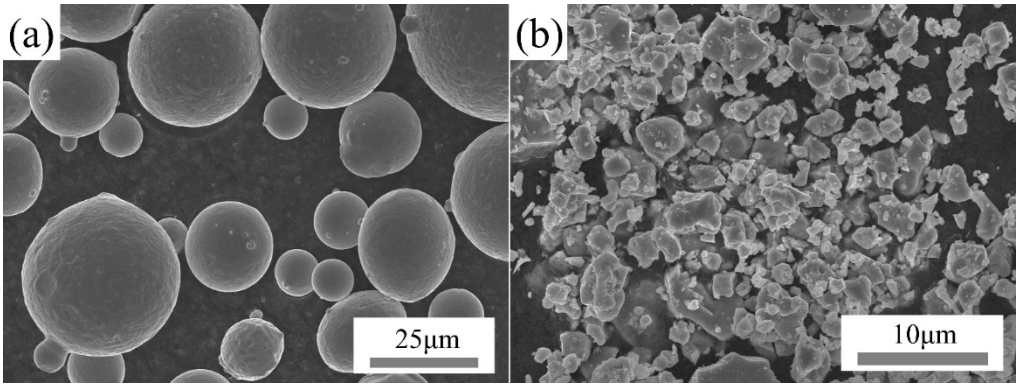

Figure 1. (**a**) gas atomized powder of Inconel 718, and (**b**) NbC flakes.

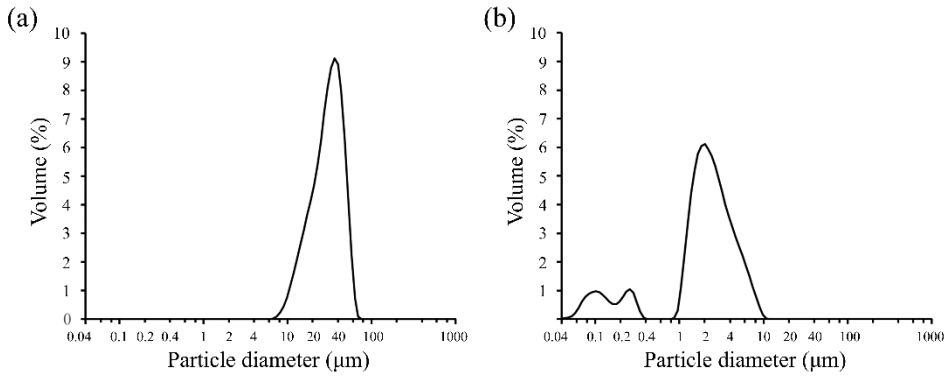

Figure 2. (**a**) powder size distribution of Incoenl 718 feedstock, and (**b**) NbC flakes.

2.2. Selective Laser Melting Process

An in-house SLM machine equipped with a ytterbium fiber laser (λ: 1070 nm, YLR-500-SM-AC, IPG Photonics Co, Oxford, MA, USA.) was used. The chamber was protected with purity 99.99% argon gas, and the oxygen content of the chamber was kept at less than 100 ppm. The baseplate was S45C steel, and the pre-heating temperature was at 200 °C. During the SLM process, zig-zag lines scanning pattern was used, the hatch distance between each scanning track was 100 μm, and the layer thickness was 50 μm. During the scanning process, each layer was rotated by 67°. SLM scanning parameters were determined in order to achieve the least fractions of porosity (0.06 vol%, which was determined by image analysis) based on sets of experiments of laser power (110 W to 280 W) and scanning speed (400 mm/s to 1200 mm/s). In this study, a laser power of 220 W and a scanning speed of 800 mm/s were employed to fabricate samples for the following experiment. For microstructure observation and heat treatment study, the specimen size was 8 mm in length and width and 6 mm in height (120 layers). For tensile specimens, the samples were 15 mm in width, 90 mm in length, and 8 mm in height (160 layers).

2.3. Post-SLM Heat Treatment

The as-built parts were removed from the baseplate by electrical discharge machining. Two types of post-heat treatments were performed. The first type consisted of a solution heat treatment (SHT) at 1100 °C for 2 h followed by air cooling; the SHT temperature was chosen at above the δ solvus [36] in order to homogenize the chemistry [10]. After SHT, the aging process was performed to precipitate γ' and γ'', the aging heat treatment consisted

of 720 °C for 8 h, then samples were furnace cooled to 620 °C and soaked for 8 h followed by air cooling to room temperature; for the post-SLM, heat treatment consisted of SHT and aging, a designation of STA is given. The second type of post-SLM heat treatment was a direct aging process (DA), without the SHT step, DA samples were subjected to the same aging treatment as that of STA. The microstructures and properties of the STA and DA samples with varying NbC contents were compared in this work systematically.

2.4. Tensile Test

Specimens for tensile tests were sectioned perpendicularly to the building direction and the gage section dimension followed the ASTM standard E8/E8M [37]. All surfaces of specimens were ground with 2000 grit SiC sandpaper prior to tensile tests. All tests were conducted at ambient temperature by a tensile test machine (INSTRON 4468, Instron, Norwood, MA, US) equipped with an extensometer; strain rate of the test was 10^{-3} per second. At least two specimens for each condition were tested and the averaged values of tensile properties are presented.

2.5. Microstructure Analysis

Specimens were ground by SiC sandpaper and then polished by 0.05 μm Al_2O_3 suspension; sample surfaces were electrolytically etched in 20 vol% phosphoric acid aqua solution. An optical microscope and a scanning electron microscope (SEM, Hitachi SU-8010, Tokyo, Japan) were used to observe microstructures; particle size, phase fraction, and inter-particle spacing were estimated by using Image J software (version 1.52a, Wayne Rasband, USA) [38]. For high-resolution analysis, transmission electron microscopy (TEM, JEOL JEM-F200, Tokyo, Japan) was employed, specimens were ground with 2000 grit SiC paper to a thickness of 50 μm and then punched into round discs with a diameter of 3 mm, discs were then polished by a twin-jet polisher in 10 vol% $HClO_4$ + 90 vol% C_2H_5OH solution under 25 volt at −30 °C. For grain texture analysis, specimens for electron back scattering diffraction (EBSD) analysis were prepared by surface polishing with Al_2O_3 suspension followed by 0.02 μm colloidal silica suspension. EBSD analysis was performed with a JEOL JSM-7610F SEM equipped with an AZtec EBSD system (Oxford Instruments, Abingdon, Oxfordshire, UK). Grain analysis was conducted with a 100× magnification image and the step size was 4 μm, misorientation analysis for plastic deformation was performed with a 250× magnification image and a step size of 1 μm. More than 200 grains were counted in each specimen; for misorientation and dislocation density analysis, the Kernel Average Misorientation (KAM) analysis was used, and original EBSD data was post-processed with the Oxford Channel 5 software (Oxford Instruments, Abingdon, Oxfordshire, UK). The averaged KAM values with different kernel radius were then used to calculate overall geometrically-necessary dislocation (GND) density according to the methodology described by Moussa et al. [39]. It has been reported that GND density is related to lattice curvature, which is corresponding to plastic deformation and crystal misorientation [40–42]; Nye's dislocation tensor can provide a relationship of GND density based on local average misorientation [41]. The GND density ρ could be estimated by Equation (1) below:

$$\rho \cong \frac{a\,\theta}{b\,x} \tag{1}$$

where θ is the average misorientation in radius, b is Burgers vector, x is the distance along which misorientation is measured, and a is 3 based on the previous literature [39,41]. The approximation was later modified by Kamaya [43] and Moussa et al. [39], where θ/x is replaced by $d\theta/dx$ to remove the background noise of the EBSD detector. Assuming that the misorientation gradient is constant around the near pixels and there is no misorientation when kernel size is 0, then misorientation θ would be proportional to the distance x. In this study, the averaged misorientation data from KAM analysis with different kernel radius were recorded. The misorientation degree to define a high angel grain boundary was chosen as 15°, and misorientation degree below 15° would be considered in KAM analysis

to separate the lattice of different grains [39,42,44]. Then the slope of the data points was calculated as $d\theta/dx$. Eventually, overall GND density could be determined based on the modified tensor in this work.

3. Results and Discussion

3.1. As-SLM Microstructures

The cross-sectional optical micrographs of as-built samples are shown in Figure 3, and the melt-pools structures are clearly visible. Melting pool depths were measured based on the final layer of the as-built sample, at least 10 melting pool depths of different sides of the as-SLM samples were observed. With NbC additions, the average depth of melt-pools decreased notably from 223.4 μm of 0% NbC to 139.4 μm with 5.0% NbC (164.9 μm for 0.5% NbC, and 159.3 μm for 1.0% NbC), Figure 3a–d. A similar observation was reported by AlMangour et al. [31]. Gu et al. [45] suggested that inclusion particles could inhibit the convection inside the melting pool, which could cause a smaller melting pool due to heat accumulation at the melting pool surface [46]. A few un-dissolved and agglomerated NbC inclusions around 15 μm were also observed; the amounts appeared to increase with higher NbC contents. High magnification micrographs of as-built samples are shown in Figure 4; sub-micron cellular dendritic structure could be observed and inter-dendritic regions could be identified as a bright cellular wall. The increase in NbC addition also appeared to decrease the average cellular size; without NbC, the average cell size was 397 nm, and it decreased to average values of 357.6 nm, 334.6 nm, and 283.8 nm for 0.5%, 1.0%, and 5.0% NbC contents, respectively, Figure 4a–d. The decreases in the depth of melt-pools and the cell size were associated with an increase in the NbC addition. The as-SLM microstructures with and without NbC all exhibited cellular dendrites instead of equiaxed dendrite, Figure 4; this kind of microstructures was a result of a high ratio of temperature gradient to solidification velocity, and could induce small degree of constitutional supercooling and the growth of cellular structure along the solidification direction [47]. It is known that the cellular wall could contain high density of dislocations because of cyclic thermal stress during the fusion process of SLM; these dislocations have been reported to contribute to strengthening [48–50]. An equation for the influence of thermal gradient and solidification velocity on dendrite arm spacing L can be described as following [51]:

$$L = \frac{a}{G^b V^c} \quad (2)$$

where G is the thermal gradient, V is the solidification velocity (velocity of liquid-solid interface), a, b and c are constants [51]. Since SLM process was performed with a small laser beam size (~58 μm), the melt-pools had high thermal gradient and fast solidification velocity, resulting in the formation of fine cellular dendrites shown in Figure 4.

TEM analysis indicated that particles presented along the cell walls in samples without NbC addition were hexagonal C14 Laves phase (lattice parameter a: 4.9 Å and c: 7.8 Å [52]), Figure 4e; by contrast, FCC_B1 Nb-rich cubic carbides (lattice parameter a: 4.4~4.5 Å [53]) were identified along cell walls for all samples with NbC additions, Figure 4f. These particles were incoherent with the FCC matrix (a: 3.58 Å based on TEM analysis). It appeared that the formation of both Laves phase and cubic carbides along cell walls were associated with Nb segregation to the interdendritic regions, as shown by the TEM-EDS analysis presented in Table 2. Furthermore, grain sizes were decreased with NbC additions, from 18.94 μm of no NbC addition to 10.51 μm of 5.0% NbC addition. Previous work indicated that small amount un-dissolved inoculants could affect the texture of grains and also decrease the grain size of as-built Inconel 718 [17], so it was possible that un-dissolved NbC in this work provided heterogeneous grain nucleation sites. Furthermore, dissolution of some NbC could also increase the amount of constitutional supercooling and provide more nucleation sites during solidification [47].

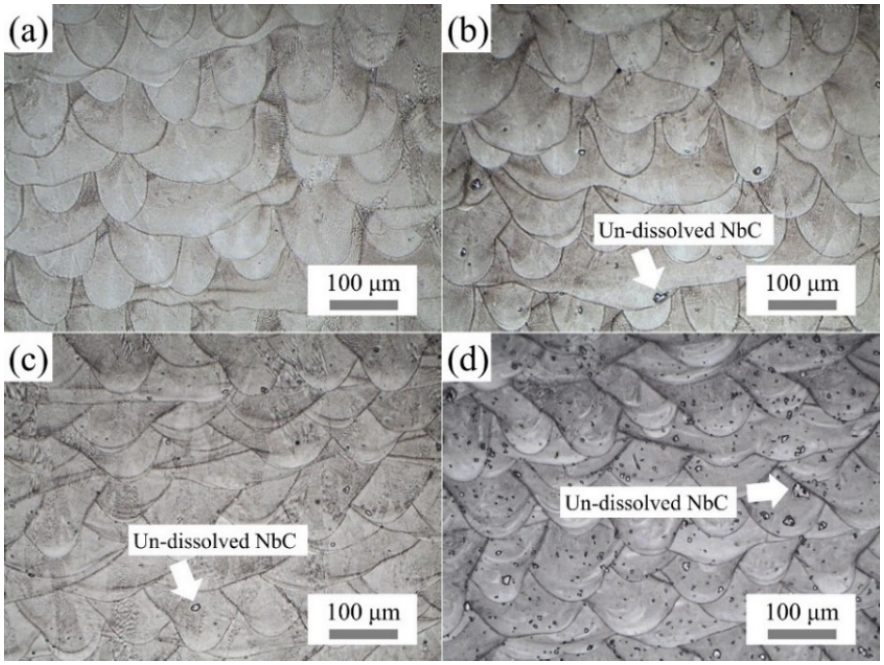

Figure 3. Cross-sectional views of melt pool morphology (**a**) without NbC, (**b**) with 0.5% NbC, (**c**) with 1.0% NbC, and (**d**) with 5.0% NbC in weight.

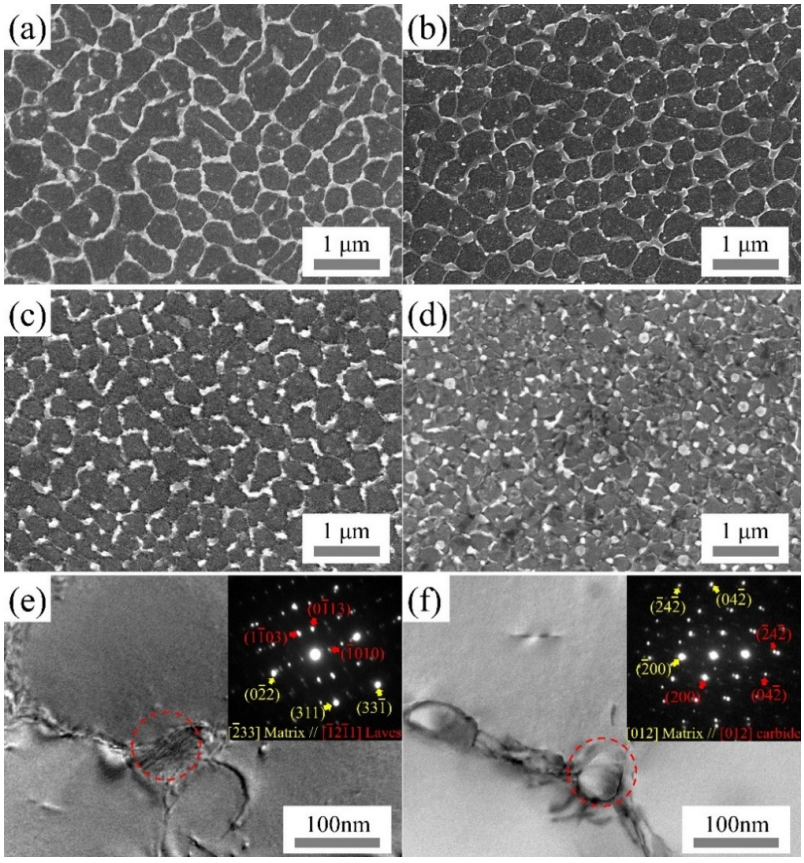

Figure 4. As-built cellular structure observed under SEI (**a**) without NbC, (**b**) with 0.5% NbC, (**c**) with 1.0% NbC, and (**d**) with 5.0% NbC in weight. TEM bright field images and diffraction patterns, (**e**) Laves phase was identified in the sample without NbC, and (**f**) cubic carbide was identified with NbC additions.

Table 2. TEM-EDS composition analysis of cellular structure and particles of as-built condition (at%).

Condition	Position	Ni	Cr	Fe	Nb	Mo	Al	Ti
Without NbC	Cellular core	51.53 ± 0.91	21.60 ± 1.29	19.05 ± 0.26	2.81 ± 0.25	2.15 ± 0.24	1.45 ± 1.03	1.18 ± 0.1
	Cellular wall	45.42 ± 0.62	18.96 ± 1.92	15.73 ± 1.97	13.43 ± 2.07	2.97 ± 1.73	1.40 ± 0.40	2.10 ± 0.70
	Laves	40.40 ± 2.01	16.40 ± 0.91	17.83 ± 1.85	15.95 ± 2.60	6.40 ± 1.74	1.45 ± 0.24	1.33 ± 0.43
With NbC (0.5%)	Cellular core	50.33 ± 0.57	22.53 ± 1.40	19.37 ± 0.90	3.43 ± 0.47	1.70 ± 0.30	1.60 ± 0.10	1.03 ± 0.27
	Cellular wall	46.25 ± 0.35	19.05 ± 1.35	15.40 ± 0.31	12.85 ± 3.05	3.15 ± 0.35	1.63 ± 0.43	1.68 ± 0.42
	Carbide	17.57 ± 6.22	12.50 ± 0.83	5.87 ± 2.00	47.22 ± 5.11	7.20 ± 2.30	1.00 ± 0.08	8.63 ± 4.20

3.2. Microstructures after Post-SLM Heat Treatments

Microstructures of the samples subjected to STA heat treatment are shown in Figure 5, and it shows that cellular walls were all eliminated; with more NbC additions, more bright particles could be observed in the microstructures, Figure 5a–d. According to the TEM diffraction pattern in Figure 5e,f and TEM-EDS analysis shown in Table 3, these particles were Nb-rich FCC_B1 cubic carbides, some large ones (430 nm~628 nm) were found along grain boundaries, while smaller particles (46~57 nm) were seen within the grain. Figure 6 shows the microstructures of samples subjected to DA heat treatment, and bright particles were observed along cellular wall; Figure 6e,f are TEM micrographs of these particles along the cellular wall, and their compositions are shown in Table 3 to compare with that in the STA specimen. TEM analysis indicated that for the specimen without NbC addition, these particles were C14 Laves phase, while with NbC addition, particles along the cellular wall were found to be Nb-rich FCC_B1 cubic carbide. The positions, volume fractions, and diameter of these particles after STA and DA treatments are shown in Table 4. Particles of STA specimens were categorized into "intragranular carbide" and "carbide along grain boundary" based on the observation in Figure 5; for DA specimens, particles along cellular wall were considered and they were identical to particles along grain boundaries. It is shown that NbC addition led to carbide formation and increased particles fraction to all specimens. For DA specimens, the volume fraction of particles increased from 1.28% to 7.6% with 5.0% NbC addition. A similar result was observed in STA specimens, volume fractions of both types of carbide increased with NbC addition, from 0.11% (intragranular carbide) and 0.09% (carbide along grain boundary) of no NbC content to 3.23% (intragranular carbide) and 4.36% (carbide along grain boundary) of 5.0% NbC. It should be noted that overall volume fractions of particles in STA specimens were less than those of DA specimen, which could be associated with more homogeneous composition profile due to STA heat treatment.

Figure 7 illustrates TEM images of precipitate in STA and DA specimens; these particles were mainly γ'' with disc-shaped morphology. Image analysis indicates that the average length along the long axis of γ'' particles was 12.8 nm for STA specimen without NbC and 12.9 nm for STA specimen with NbC additions. For DA specimen, the average length along the long axis of these particles was about 13.3 nm for DA specimen without NbC and 13.0 nm for DA specimen with NbC. It has been reported that the growth of primary strengtheners, i.e., γ' and γ'' in Inconel 718 could follow Lifshitz-Slyozovi-Wagner theory, which suggests coarsening rate can be determined by diffusivity, temperature, and solute concentration [54]. Based on the as-built chemical profile of sample without NbC addition (Table 2), although there was an obvious Nb segregation toward cell wall regions, the overall chemical compositions were not affected much by the addition of NbC. With the same aging treatment, it is expected that DA samples and STA samples possessed virtually identical sizes and fractions of primary strengtheners.

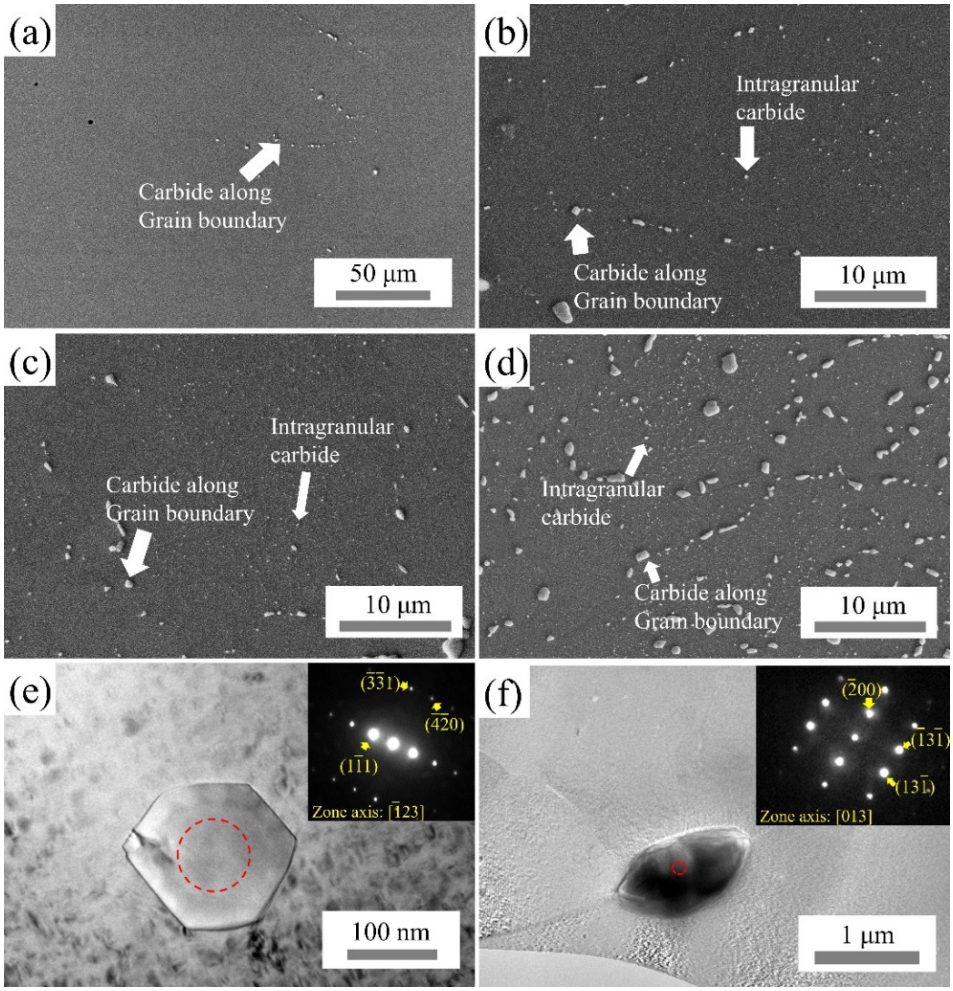

Figure 5. Microstructure of specimens after STA. (**a**) Without NbC, (**b**) 0.5% NbC, (**c**) 1.0% NbC, and (**d**) 5.0% NbC. (**e**) TEM bright field image of the specimen without NbC; diffraction pattern of carbide particle. (**f**) TEM bright field image of the specimen with 0.5% NbC; diffraction pattern of carbide particle.

Table 3. TEM-EDS analysis of particles along cellular wall after post-SLM heat treatments (at%).

Treatment	Condition	Ni	Cr	Fe	Nb	Mo	Al	Ti
STA	Without NbC	5.45 ± 0.44	3.25 ± 0.15	2.67 ± 0.21	67.26 ± 1.55	-	0.75 ± 0.45	20.71 ± 1.41
	With NbC (0.5%)	6.60 ± 0.50	3.43 ± 0.26	2.67 ± 0.21	68.83 ± 0.17	1.17 ± 0.17	0.3 ± 0.08	17.00 ± 0.96
DA	Without NbC	29.76 ± 0.78	19.93 ± 1.50	18.83 ± 0.66	15.00 ± 3.14	15.57 ± 2.09	-	0.87 ± 0.12
	With NbC (1.0%)	8.53 ± 0.50	11.97 ± 1.96	3.47 ± 0.09	58.9 ± 2.81	5.03 ± 0.29	1 ± 0.08	8.63 ± 4.20

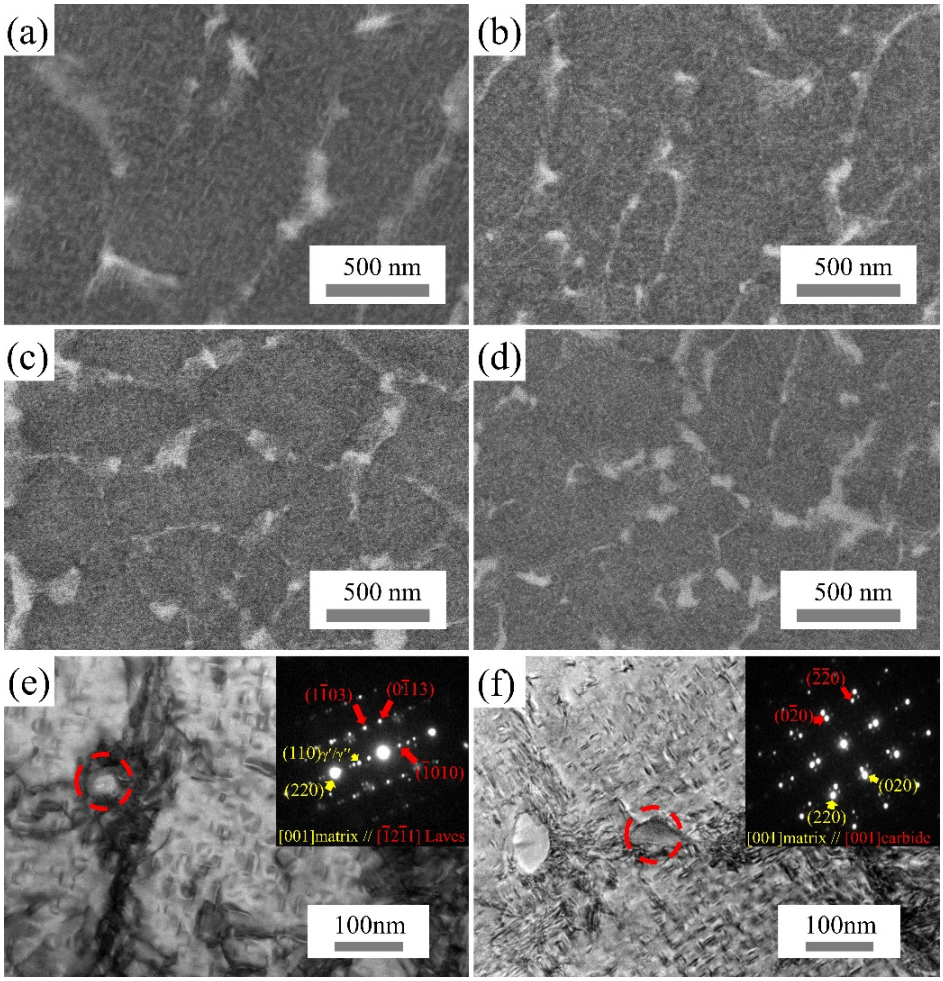

Figure 6. Microstructure of specimens after DA. (**a**) Without NbC, (**b**) 0.5% NbC, (**c**) 1.0% NbC, and (**d**) 5.0% NbC. (**e**) TEM bright field image of the specimen without NbC. diffraction pattern of hexagonal Laves phase. (**f**) TEM bright field image of particle in the specimen with 1% NbC; diffraction pattern of carbide particle.

Table 4. Volume fractions and average diameters of Laves/carbide after different heat treatments.

Condition	Treatment	Site	Volume Fraction	Average Diameter
Without NbC	STA	Intragranular carbide	0.11%	47.4 nm
		Grain boundary carbide	0.09%	544.3 nm
	DA	Cellular wall Laves	1.28%	35.3 nm
0.5% NbC	STA	Intragranular carbide	0.53%	46.0 nm
		Grain boundary carbide	0.71%	458.8 nm
	DA	Cellular wall carbide	2.54%	32.6 nm
1.0% NbC	STA	Intragranular carbide	0.80%	57.0 nm
		Grain boundary carbide	0.93%	519.3 nm
	DA	Cellular wall carbide	3.61%	32.3 nm
5.0% NbC	STA	Intragranular carbide	3.23%	51.1 nm
		Grain boundary carbide	4.36%	628 nm
	DA	Cellular wall carbide	7.60%	42.5 nm

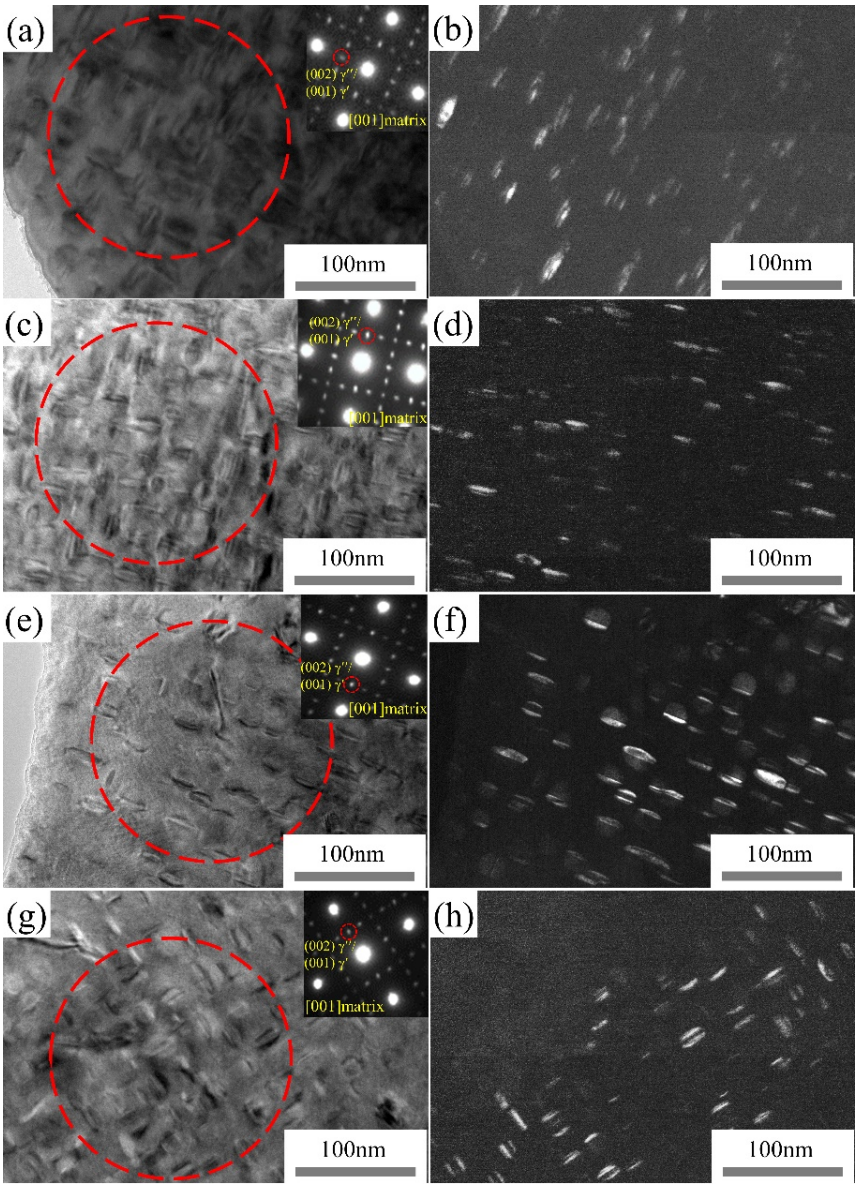

Figure 7. TEM analysis of γ'/γ'' precipiate after post-treatment. (**a**) Bright field image and diffraction pattern of STA without NbC, and (**b**) Dark field image of STA without NbC. (**c**) Bright field image and diffraction pattern of STA with 0.5% NbC, and (**d**) dark field image of STA with 0.5% NbC. (**e**) Bright field image and diffraction pattern of DA without NbC, and (**f**) Dark field image of DA without NbC. (**g**) Bright field image and diffraction pattern of DA with 1% NbC, and (**h**) Dark field image of DA with 1% NbC.

EBSD grain analysis are shown in Figure 8. Epitaxial grains growth was present in as-built Inconel 718 with NbC addition, and columnar grains were observed. However, with NbC addition, more small grains were detected. Table 5 shows the average grain diameter after different heat treatments. The average grain diameter of the as-built SLM samples decreased from 18.94 μm to 17.97 μm, 17.11 μm, and 10.51 μm for 0%, 0.5%, 1.0%, and 5.0% NbC addition, respectively. For specimens subjected to post-SLM heat treatments, it is found that STA could eliminate the columnar grains of as-built specimens and led to obvious grain growth. The average grain diameter of the sample without NbC addition was 44.53 μm after STA. It is found that grain growth during STA was inhibited with more NbC addition. Average grain size of STA specimens decreased to 30.85 μm with 0.5% NbC, 21.53 μm with 1.0% NbC, and 13.45 μm with 5.0% NbC addition. On the other hand, DA

had less influence on grain size and grain morphology; grain structures of DA specimens were similar to those of as-built conditions.

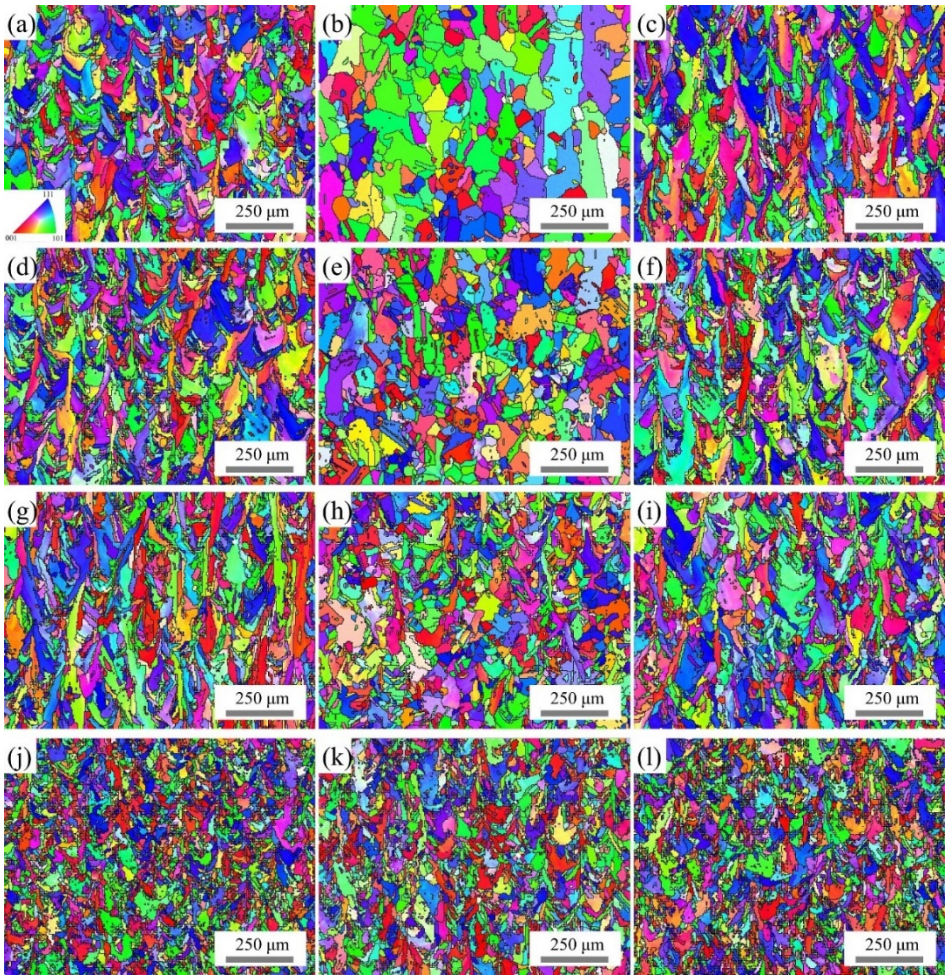

Figure 8. Overall EBSD inverse pole figures of different specimens. (**a**) as-built without NbC, (**b**) STA without NbC, (**c**) DA without NbC, (**d**) as-built with 0.5% NbC, (**e**) STA of 0.5% NbC, (**f**) DA of 0.5% NbC, (**g**) as-built of 1.0% NbC, (**h**) STA of 1.0% NbC, (**i**) DA of 1.0% NbC, (**j**) as-built of 5.0% NbC, (**k**) STA of 5.0% NbC, and (**l**) DA of 5.0% NbC.

Table 5. Average grain diameter of different specimens.

Condition	As-Built	STA	DA
Without NbC	18.94 μm	44.53 μm	19.90 μm
0.5% NbC	17.97 μm	30.85 μm	18.57 μm
1.0% NbC	17.11 μm	21.53 μm	18.26 μm
5.0% NbC	10.51 μm	13.45 μm	11.11 μm

The overall GND densities of different specimens have been estimated by the method described in Section 2.5 and results are presented in Table 6. The corresponding KAM maps are shown in Figure 9. All the as-built specimens had similar GND density around $4.04 \times 10^{13}/m^2$~$4.54 \times 10^{13}/m^2$ and the values were independent of the contents of NbC addition. After STA heat treatment, GND density decreased from $4.18 \times 10^{13}/m^2$ to $1.31 \times 10^{12}/m^2$ for samples without NbC addition. GND density of STA specimens with NbC additions also decreased significantly due to stress relief by SHT. By contrast, DA processes did not appear to decrease the GND density dramatically for all specimens with and without NbC additions.

Table 6. Overall GND density of different specimens.

Condition	As-Built	STA	DA
Without NbC	4.18×10^{13} /m^2	1.31×10^{12} /m^2	4.32×10^{13} /m^2
0.5% NbC	4.06×10^{13} /m^2	2.84×10^{12} /m^2	4.05×10^{13} /m^2
1.0% NbC	4.54×10^{13} /m^2	1.74×10^{13} /m^2	4.35×10^{13} /m^2
5.0% NbC	4.04×10^{13} /m^2	3.62×10^{13} /m^2	3.87×10^{13} /m^2

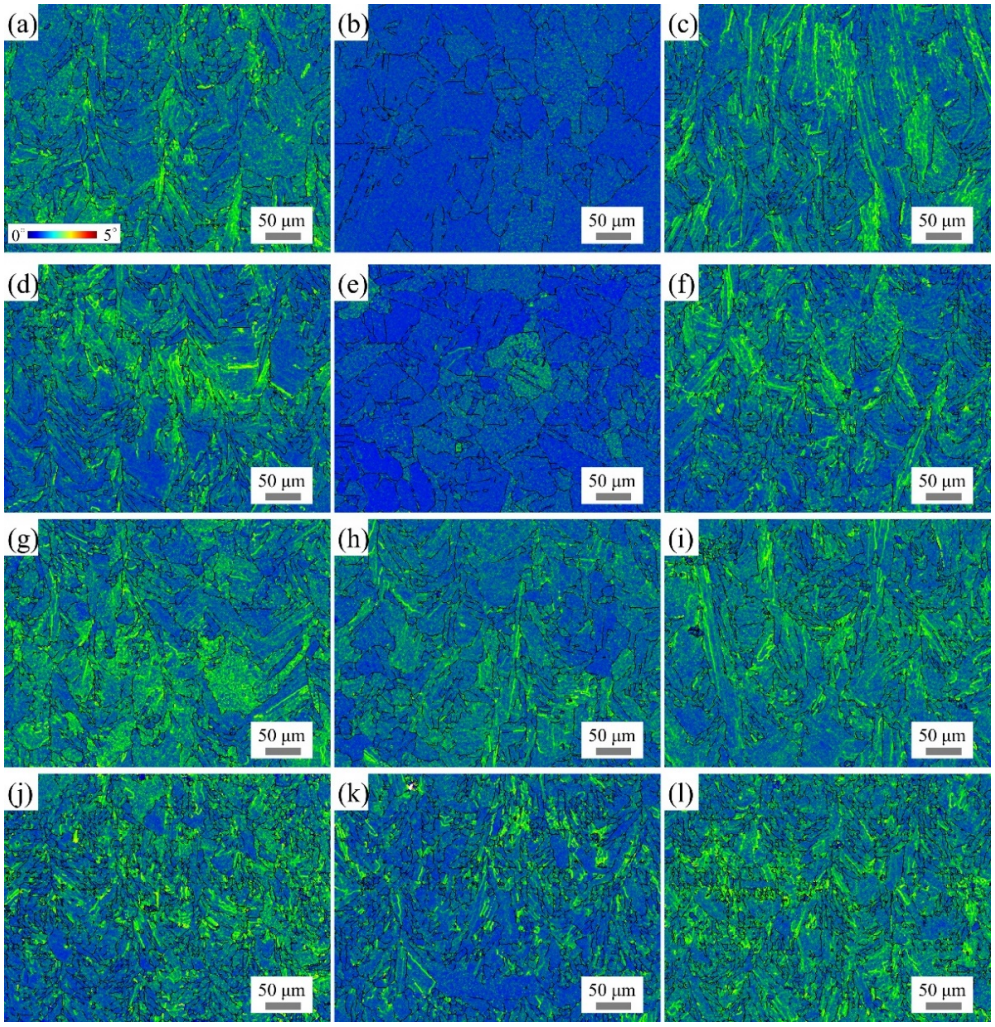

Figure 9. KAM map of different specimens. (**a**) as-built without NbC, (**b**) STA without NbC, (**c**) DA without NbC, (**d**) as-built with 0.5% NbC, (**e**) STA of 0.5% NbC, (**f**) DA of 0.5% NbC, (**g**) as-built of 1.0% NbC, (**h**) STA of 1.0% NbC, (**i**) DA of 1.0% NbC, (**j**) as-built of 5.0% NbC, (**k**) STA of 5.0% NbC, and (**l**) DA of 5.0% NbC.

3.3. Tensile Properties

Tensile stress and strain curves are presented in Figure 10, and the corresponding tensile properties are listed in Table 7. For STA specimens, yield strength (YS) and ultimate tensile strength (UTS) increased gradually with NbC additions, from 1134.8 MPa and 1359.9 MPa of no NbC addition, to 1325.5 MPa and 1498.4 MPa of 5.0% NbC, respectively. After DA process, tensile strengths of samples increased significantly and the influence of NbC addition was more pronounced. Without NbC addition, YS was 1357.5 MPa and UTS was 1490.4 MPa; with 0.5% NbC addition, YS was 1461.0 MPa and UTS was 1575.2 MPa. However, for DA specimens with NbC addition of more than 1.0%, both YS and UTS were decreased compared to that of 0.5% NbC. DA specimen with 5.0% NbC addition

broke without reaching the yield point. For samples without NbC addition, the elongation decreased from 23.96% to 14.59%. The elongation further decreased to 9.95% and less for samples with NbC additions greater than 1.0%. Tensile properties of as-built and as-SHT specimens without NbC addition, and as-built specimen with 0.5% NbC, are also listed in Table 7. As-built specimen without NbC had a YS of 771.6 MPa, and 0.5% NbC addition could increase the YS to 841.4 MPa in as-built condition, while as-SHT specimen with no NbC exhibited a YS of 379.5 MPa and large elongation.

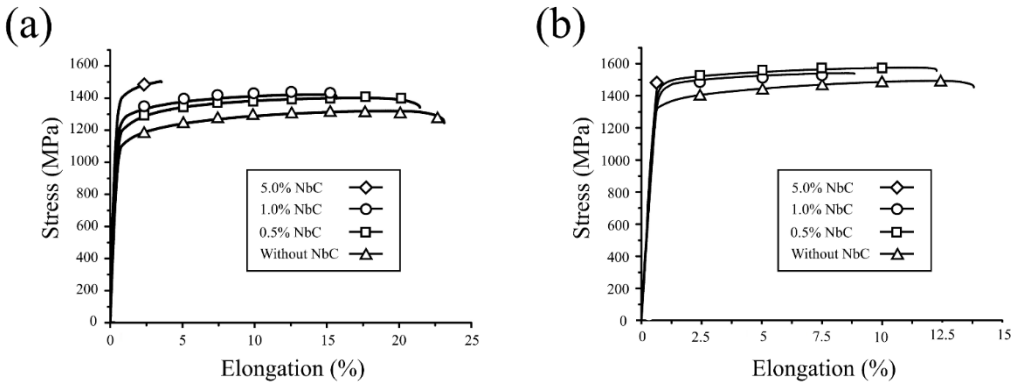

Figure 10. Room temperature tensile stress-strain curves (**a**) STA specimens and (**b**) DA specimens.

Table 7. Tensile properties of specimens in this study.

Condition	Treatment	YS (MPa)	UTS (MPa)	E (GPa)	Elongation%	Strain Hardening Exponent *n*
Without NbC	As-built	771.6 ± 3.2	1031.5 ± 5.2	200.04 ± 13.7	25.94 ± 0.14	0.1230 ± 0.0048
	SHT	379.5 ± 6.4	876.2 ± 9.7	205.3 ± 7.7	61.02 ± 0.67	0.2162± 0.0091
	STA	1134.8 ± 4.8	1312.5 ± 3.3	200.0 ± 7.0	23.86 ± 1.19	0.1001 ± 0.0032
	DA	1357.5 ± 2.5	1490.4 ± 3.4	223.0 ± 3.0	14.59 ± 4.45	0.0796 ± 0.0041
0.5% NbC	As-built	841.4 ± 0.35	1105.9 ± 1.1	212.8 ± 3.2	20.62 ± 0.77	0.1199 ± 0.0035
	STA	1175.7 ± 20.4	1395.3 ± 3.3	205.2 ± 17.9	20.40 ± 0.50	0.0968 ± 0.0004
	DA	1461.0 ± 2.5	1575.2 ± 0.2	219.2 ± 10.0	10.45 ± 0.19	0.0679 ± 0.0011
1.0% NbC	STA	1221.6 ± 5.4	1423.8 ± 2.2	214.2 ± 20.8	9.95 ± 1.45	0.0850 ± 0.0006
	DA	1439.5 ± 16.5	1545.3 ± 4.4	212.5 ± 1.3	6.80 ± 1.43	0.0541 ± 0.0027
5.0% NbC	STA	1325.5 ± 35.5	1498.4 ± 5.4	235.0 ± 1.0	3.33 ± 0.03	0.0654 ± 0.0002
	DA	Broke before YS	1412.8 ± 85.2	213.8 ± 1.3	-	-

Stress-strain curves were used to calculated strain hardening exponents (n) based on the Hollomon equation below [55], n values are listed in Table 7.

$$\sigma_t = k\varepsilon_t^n \tag{3}$$

where σ_t is the true stress, ε_t is the true strain, k is the strength coefficient, and n is strain hardening exponent. n is the gradient by plotting σ_t vs. ε_t in logarithmic scale. It is found that strain hardening exponents decreased with NbC additions, and STA samples possessed higher n values than that of DA samples. Fracture surfaces of tensile specimens are shown in Figures 11 and 12. Dimples were observed in the matrix at most of the regions of fracture surfaces, and this suggests that the fracture of FCC matrix was ductile. However, some brittle fracture features were observed in the specimens with NbC additions. It was clear that cracks were formed associated with carbide particles; most of these cracked carbide particles with irregular morphology were the residual NbC flakes shown in Figure 3. The fracture surfaces of DA specimens were similar to the STA specimens without NbC addition.

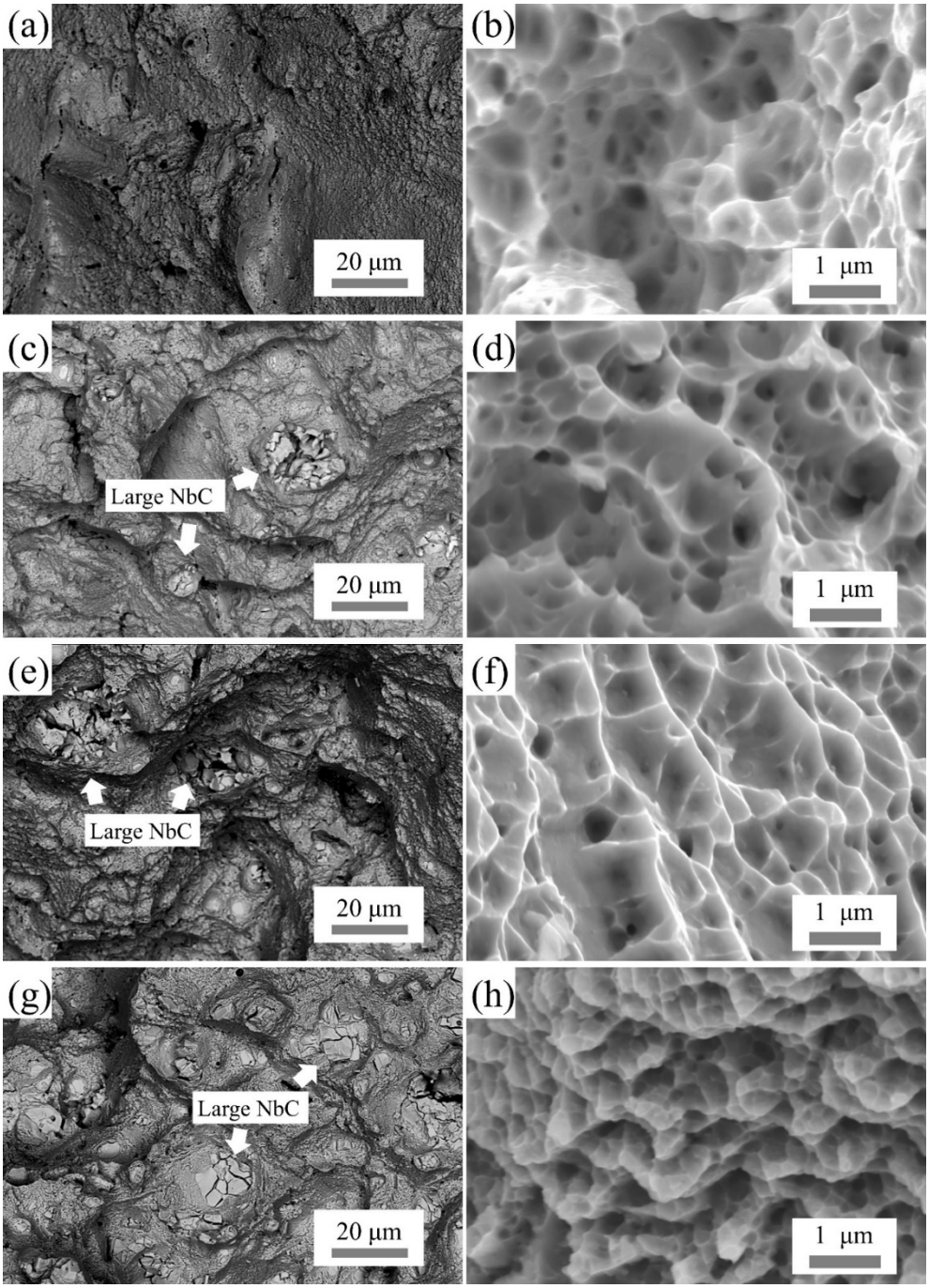

Figure 11. Fracture surfaces of STA specimens. (**a**,**b**) without NbC, (**c**,**d**) 0.5% NbC, (**e**,**f**) 1.0% NbC, and (**g**,**h**) 5.0% NbC.

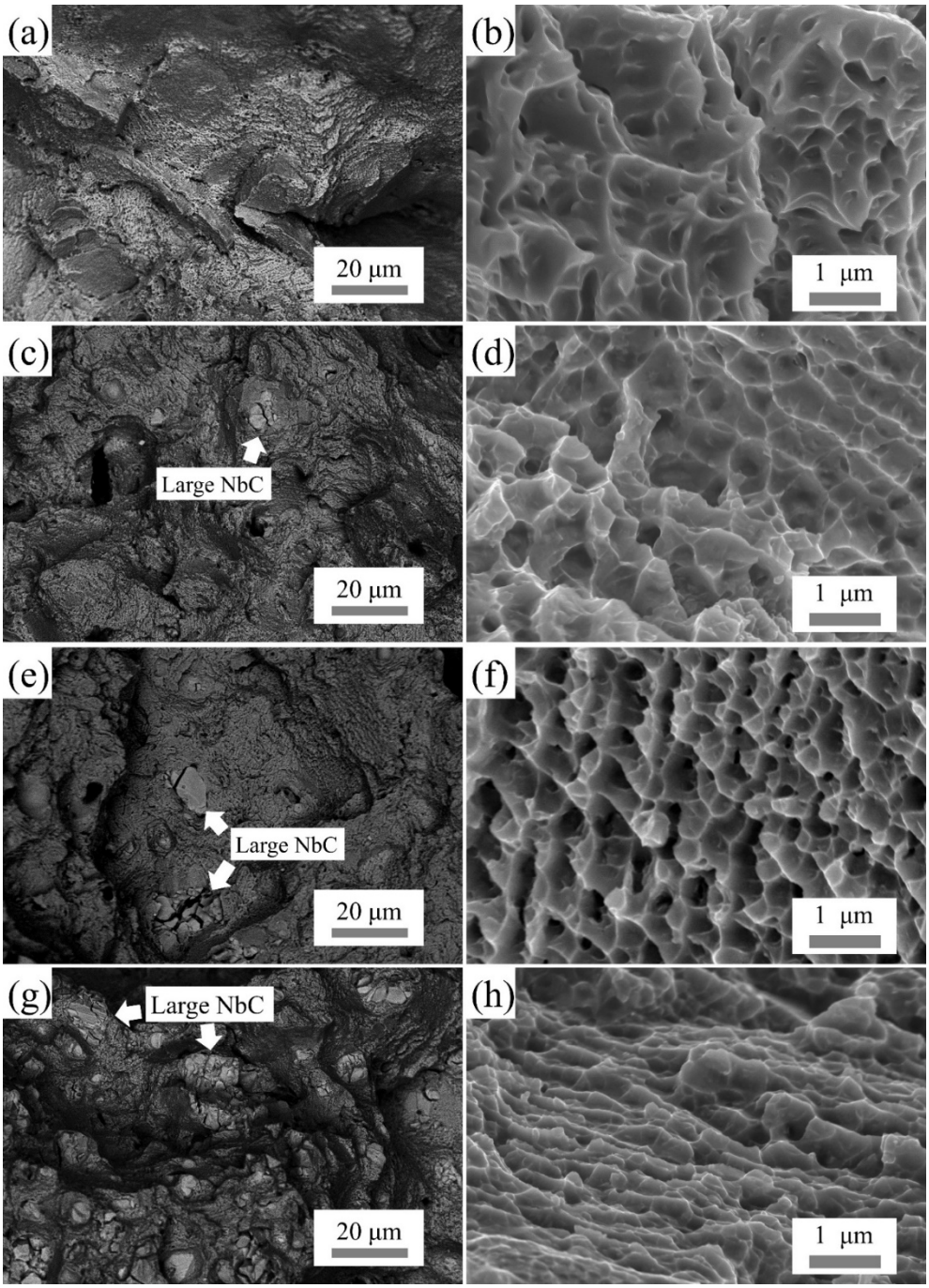

Figure 12. Fracture surfaces of DA specimens. (**a**,**b**) without NbC, (**c**,**d**) 0.5% NbC, (**e**,**f**) 1.0% NbC, and (**g**,**h**) 5.0% NbC.

Results of tensile tests indicated that DA samples could exhibit higher strength than those of STA samples, as shown in Figure 10, and NbC addition further increased the strength of specimens. However, degradations of strength and ductility were observed in DA specimens when NbC addition was more than 1.0%; brittle fracture occurred on large NbC particles shown in Figures 11 and 12 were responsible for this observation. It should be noted that fracture particles larger than 10μm had multiple boundaries inside, which could also indicate that these were agglomeration of small flakes. These large NbC particles or agglomerations became stress concentration sites for brittle fracture; they broke during the tensile test, decreased the load-bearing volume. According to fracture toughness mechanism [56], DA specimens were less ductile than STA specimens because

they possessed high GND density, and stress in tension could trigger the propagation of crack along un-dissolved NbC particles without significant yielding. Because fractions of un-dissolved NbC increased with more NbC addition as shown in Figure 3, this could lead to the degradation of mechanical properties for specimens with higher NbC contents. Analysis showed that strain hardening exponent decreased with both NbC additions and DA process, Table 7. DA specimens had higher GND density prior to tensile test, and this implied DA specimens had been strain-hardened; hence, it could result in lower strain hardening rates and elongations. However, UTS of these DA specimens were still higher than those of STA specimens. Hence the significant strengthening in tension achieved in this work could be mainly attributed to the increase in yield strength. In the following section, 0.5% NbC specimen has been chosen for further discussion about each strengthening contributions in order to avoid the influence of un-dissolved NbC particles.

There are several factors that could affect the yield strength of alloy, and they can be expressed as the following equation [23,30,57]:

$$\sigma_y = \sigma_0 + \left(\sigma_{G.B}^k + \sigma_{strain}^k + \sigma_{r'}^k + \sigma_{r''}^k \ldots\right)^{1/k} \quad (4)$$

where σ_y is the YS of material. σ_0 is the strengthening contribution of matrix, and this term includes solid solution strengthening, stacking fault strengthening, friction stress [29–31]. Other strengthening contributions include grain boundary $\sigma_{G.B}$, precipitation $\sigma_{\gamma'}/\sigma_{\gamma''}$, and strain hardening σ_{strain}. The exponent k is a constant depending on the interaction between each factor [57]. As shown in Figure 8 and Table 5, grain size changed with NbC content and heat treatment. Variation of grain size could influence tensile strength according to Hall-Petch relation; grain boundary could inhibit the movement of dislocation and hence smaller grains could provide higher strength to material [56]. The relationship is expressed as the equation below:

$$\sigma_{G.B.} = \frac{K}{\sqrt{d}}, \quad (5)$$

where d is grain diameter of matrix and K is Hall-Petch coefficient related to material properties. Here, K is chosen as 750 MPa $\mu m^{1/2}$ for superalloy [58]. The average grain size in Table 5 was used. Calculated strengthening contribution of grain boundary to STA specimens was 112.4 MPa for specimen without NbC, and the value increased to 135 MPa with 0.5% NbC addition. NbC addition also increased the strengthening contribution of grain boundary to DA specimen slightly, from 168 MPa to 174 MPa of 0.5% NbC addition. It is known that GND density could dominate the plastic deformation and working hardening of SLM FCC materials [48], and it has also been reported that working hardening could increase proportionally with GND density [42]. Assuming that residual strain of SLM components would not cause large distortion, then GND density data from Table 6 could be used to estimate strengthening contribution by Taylor equation, which was used in previous studies [30,59,60]. Taylor relation describes necessary shear stress to overcome stress field between each dislocation. The equation is described below [56]:

$$\sigma_{Strain} = \alpha\, M\, G\, b\sqrt{\rho} \quad (6)$$

where M is Taylor factor (3 is assumed in this study), G is the shear modulus of the matrix (76 GPa based on previous work [58]), b is Burgers vector, and α is a value depending on the dislocation distribution. For heterogeneous distribution such as cellular structure, in which dislocations are accumulated along the cellular wall, α value of 0.3 was used in this study [59].

Estimated strengthening contribution of dislocation to STA specimens was 19.9 MPa for specimen without NbC and the value increased with 0.5% NbC addition to 29.3 MPa because that Zener drag could preserve some dislocation during heat treatment. On the other hand, NbC addition had less influence on strengthening contribution of dislocation to DA specimens. The strengthening contribution of dislocation to DA specimens was

110.5~117.7 MPa and was independent of NbC addition based on GND density data in Table 6. Strengthening contribution of dislocation from thermal strain in this study was lower than previous literatures of other fused based AM processes [29–31,48], in which strengthening contribution of dislocation about 160~400 MPa was reported. It might be because a relatively low energy density and pre-heating baseplate were used in this study, and both could decrease the thermally induced stress during the SLM process [61].

To estimate the strengthening contribution of primary strengtheners, i.e., γ' and γ'' precipitates, the following equation was used to describe the stress needed to cut through the particles [62]:

$$\sigma_{\gamma'/\gamma''} = M \frac{\gamma_{APB}}{2b} \left[\sqrt{\frac{3\,\gamma_{APB}\,f\,d}{\pi\,T}} - f \right] \quad (7)$$

where γ_{APB} is the anti-phase boundary energy (~175 mj/m^2 for γ' and ~296 mj/m^2 for γ'' [63]), b is Burgers vector, f is the volume fraction of the particle, d is the particle diameter, T is a tension equal to $Gb^2/2$, and G is the shear modulus of the matrix. In this study, long axis diameter of particles shown in Figure 7 is chosen as diameter to simplify the calculation (~13 nm).

It is hard to determine the volume fractions of γ' and γ'' even with TEM images. Previous work used phase compositions to estimate the fraction of each phase in Inconel 718 [23]. For DA specimen, γ'' fraction was about 13.9 vol% and γ' fraction was 5.13 vol%; for STA specimens, γ'' fraction was about 16.9 vol% and γ' fraction was 5.37 vol%. NbC addition did not influence the fractions and sizes of γ' and γ'' particles; the strengthening contributions of γ'' and γ' to STA specimen were about ~596 MPa and ~173 MPa, respectively. Moreover, for DA process, the values slightly decreased to ~565 MPa and ~170 MPa, respectively.

An extra factor termed "cellular structure strengthening" (σ_{cell}) has been introduced in this work in order to describe the extra strength of DA specimen. This factor is a combination of sub-grain boundary associated with cell structure and hard particles (Laves and carbide) along cellular wall. The exponent k in Equation (4) was adjusted based on the assumptions below: (1) DA specimens and corresponding as-built specimens had similar σ_{cell} and (2) the estimated YS was close to the experimental data. The deduction gave an exponent k ~1.11, which is close to that of previous work (1.14~1.17) [23]. Hence, each strengthening contributors of STA and DA specimens can be presented in Figure 13. Based on the deduction, it is shown that for DA specimens, in addition to primary strengtheners, grain refinement and residual strain, cellular structure could provide further strengthening to Inconel 718. Without NbC addition, DA process could increase the yield strength by 222.7 MPa compared to that of STA without NbC content; with 0.5% NbC, an increase of 326.2 MPa was achieved. Based on the deduction, it is shown that for DA specimens, in addition to primary strengtheners, grain refinement and residual strain, cellular structure could provide further strengthening to Inconel 718. Since the STA process removed the cells while DA process preserved the cellular structure, NbC addition could further refine cell size and strengthen the cell walls; hence, a significant increase in yield strength beyond 1400 MPa could be achieved.

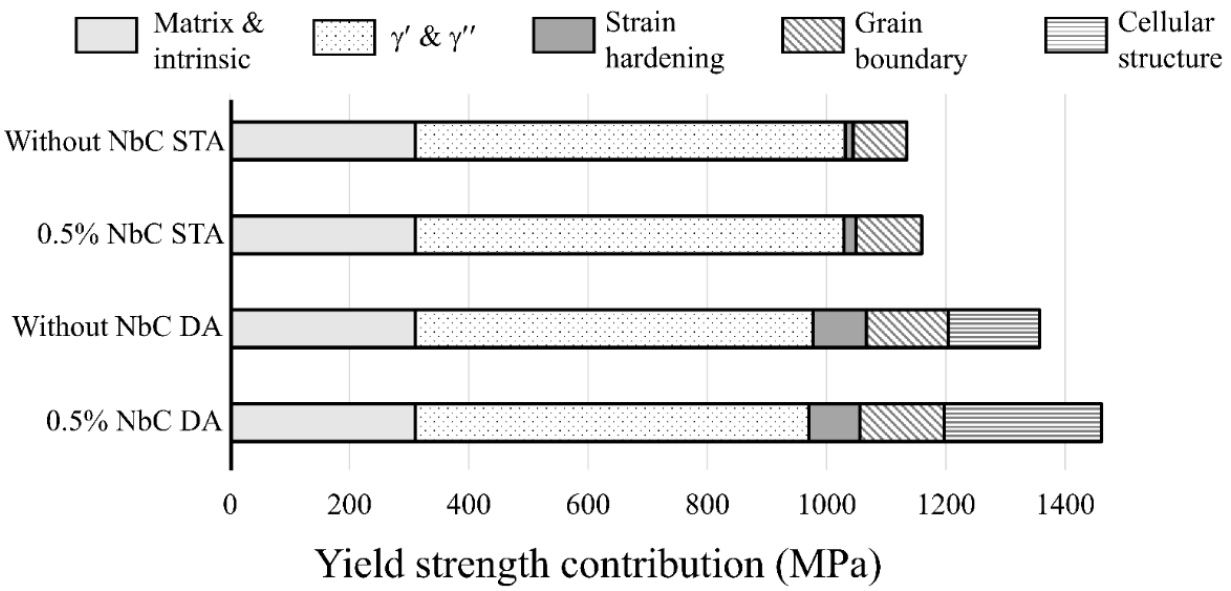

Figure 13. Contributing factors to yield strengths in samples with and without NbC addition (STA and DA heat treatments).

3.4. Comparison with Current State of the Art

Figure 14 summaries the yield strengths of Inconel 718 processed by different laser fused-based AM processes (SLM & LENS) reported in literatures. Data of cast & wrought (C&W) Inconel 718 (AMS standard 5663) is also included in the figure [64]. The wide variation in yield strengths was attributed to not only different AM processes but also different post-heat treatments. SLM process can induce higher strength than that of LENS due to faster cooling rate, and this could induce higher GND density for strain hardening and finer grain size for grain boundary strengthening. With DA process, the yield strengths of both SLM and LENS processed Inconel 718 could be enhanced. Although SHT is usually applied on traditional wrought ingots of Inconel 718, and this could relieve the internal strain and chemical segregation, direct aging could preserve the plastic strain and have less influence on the grain structure and cellular dendrites, which was responsible for significant strengthening contribution in this study. Furthermore, with NbC addition, the cell size was refined and further strengthened by nano carbides along the cell walls. It was reported by Chen et al. [8] that a tensile yield strength beyond 1400 MPa could only be achieved by traditional wrought processes with 20% plastic reduction and DA treatment, but such process would be difficult to be applied to fabricate component with complex geometry. Thus, by blending only 0.5% NbC, and with direct aging treatment, this work presents a simple but effective method to achieve high strength for Inconel 718 processed by SLM; a record-high yield strength of 1461 MPa and ultimate tensile strength of 1575.2 MPa have been achieved according to literature data to-date.

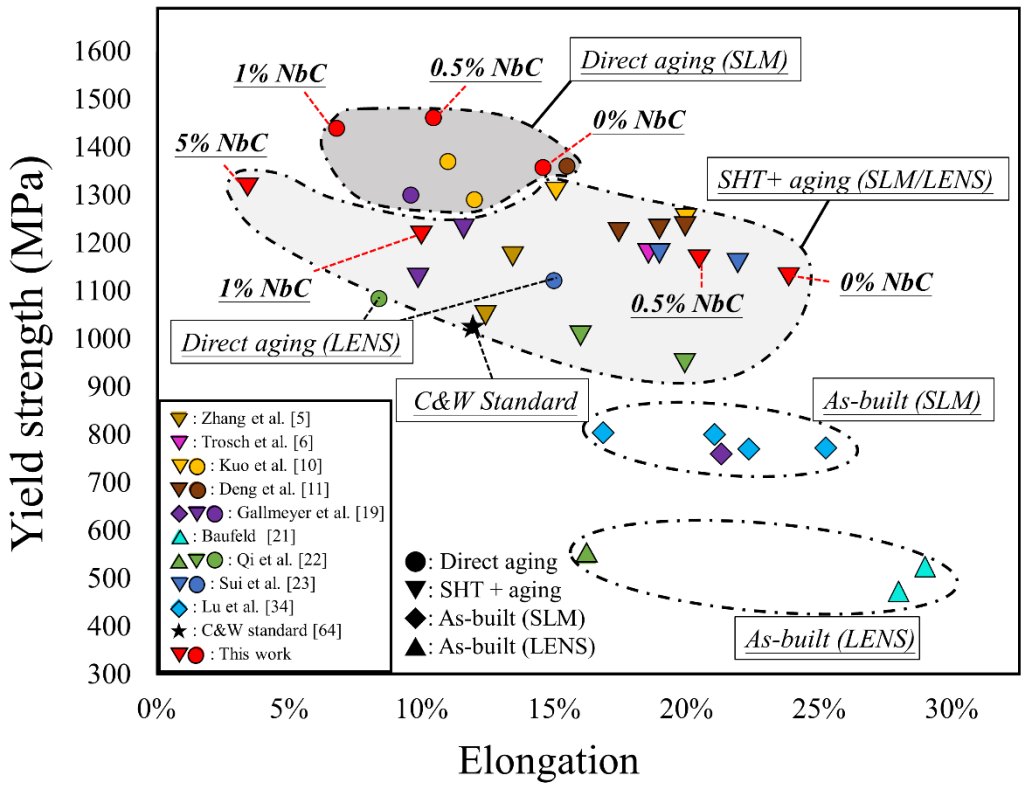

Figure 14. Yield strength of fused-based AM Inconel 718 in this work compared with literature data from [5,6,10,11,19,21–23,34,64].

4. Conclusions

An effective method to strengthen a superalloy processed by SLM has been presented; a minor amount of NbC was blended with Inconel 718 superalloy for SLM process. The post-SLM direct aging heat treatment could render up to 326.2 MPa increase in yield strength. Both grain size and cellular dendrite became finer with more NbC additions in as-SLM condition. Two types of post-SLM heat treatments were investigated, i.e., solution heat treated plus aging and direct aging. Experimental results indicate that STA treatment could eliminate the cellular dendrites, reduce residual strain, and also induce grain growth; while DA treatment could retain the as-built cellular dendrites and grain size. Both STA and DA could promote the precipitations of primary strengtheners; furthermore, with NbC additions, nano carbides precipitations were observed along the retained cellular dendritic walls in DA samples. This could provide additional Zener dragging at the refined cellular walls, which were absent in STA samples. Furthermore, it was found that additions of 1.0% and 5.0% NbC could render a significant drop in ductility due to insufficient fusion of some large NbC flakes, and 0.5% NbC addition was found to provide the highest tensile strength with moderate tensile ductility around 10%. A record yield strength of 1461 MPa and ultimate tensile strength of 1575.2 MPa for Inconel 718 processed by laser manufacturing process have been achieved in this work according to literature data to-date.

Author Contributions: Experiment, K.-C.C., M.-Y.L., T.-H.H., Y.-J.C. and K.-C.L.; writing—original draft preparation, K.-C.C.; writing—review and editing, A.-C.Y. and H.S.K.; supervision: A.-C.Y. and K.-K.J. All authors have read and agreed to the published version of the manuscript.

Funding: This research was funded by Ministry of Science and Technology (MOST) in Taiwan under Grant MOST 110-2221-E-007-020-MY3, MOST 110-2224-E-007-001, and MOST 109-2634-F-007-024.

Institutional Review Board Statement: Not applicable.

Informed Consent Statement: Not applicable.

Data Availability Statement: The data presented in this study are available on request from the corresponding author.

Acknowledgments: Authors would like to acknowledge funding supports from Ministry of Science and Technology (MOST) in Taiwan under Grant MOST 110-2221-E-007-020 -MY3, MOST 110-2224-E-007-001, and MOST 109-2634-F-007 -024; the "High Entropy Materials Center" from The Featured Areas Research Center Program within the framework of the Higher Education Sprout Project by the Ministry of Education.

Conflicts of Interest: The authors declare no conflict of interest.

References

1. Bhavsar, R.B.; Collins, A.; Silverman, S. Use of Alloy 718 and 725 in Oil and Gas Industry. In Proceedings of the Fifth International Symposium on Superalloys 718, 625, 706, and Derivatives, Pittsburgh, PA, USA, 17–20 June 2001; pp. 47–55. [CrossRef]
2. DeBarbadillo, J.J.; Mannan, S.K. Alloy 718 for Oilfield Applications. *JOM* **2012**, *64*, 265–270. [CrossRef]
3. Radavich, J.F. The Physical Metallurgy of Cast and Wrought Alloy 718. In Proceedings of the Superalloys 2004: Tenth International Symposium on Superalloys 718, 625, 706, and Derivatives, Champion, PA, USA, 19–23 September 2004; pp. 229–240. [CrossRef]
4. Private Communication with China Steel Corporation. 2014.
5. Zhang, D.; Feng, Z.; Wang, C.; Wang, W.; Liu, Z.; Niu, W. Comparison of microstructures and mechanical properties of Inconel 718 alloy processed by selective laser melting and casting. *Mater. Sci. Eng. A* **2018**, *724*, 357–367. [CrossRef]
6. Trosch, T.; Strößner, J.; Völkl, R.; Glatzel, U. Microstructure and mechanical properties of selective laser melted Inconel 718 compared to forging and casting. *Mater. Lett.* **2016**, *164*, 428–431. [CrossRef]
7. Mukhtarov, S.K. Effect of Grain Size on the Superplastic Behavior of a Nanostructured Nickel-Based Superalloy. *Mater. Sci. Forum* **2009**, *633–634*, 569–575. [CrossRef]
8. Chen, Y.-T.; Yeh, A.-C.; Li, M.-Y.; Kuo, S.-M. Effects of processing routes on room temperature tensile strength and elongation for Inconel 718. *Mater. Des.* **2017**, *119*, 235–243. [CrossRef]
9. Praveen, K.V.U.; Sastry, G.V.S.; Singh, V. Work-Hardening Behavior of the Ni-Fe Based Superalloy IN718. *Metall. Mater. Trans. A* **2008**, *39*, 65–78. [CrossRef]
10. Kuo, Y.-L.; Kamigaichi, A.; Kakehi, K. Characterization of Ni-Based Superalloy Built by Selective Laser Melting and Electron Beam Melting. *Metall. Mater. Trans. A* **2018**, *49*, 3831–3837. [CrossRef]
11. Deng, D.; Peng, R.L.; Brodin, H.; Moverare, J. Microstructure and mechanical properties of Inconel 718 produced by selective laser melting: Sample orientation dependence and effects of post heat treatments. *Mater. Sci. Eng. A* **2018**, *713*, 294–306. [CrossRef]
12. Ho, I.-T.; Chen, Y.-T.; Yeh, A.-C.; Chen, C.-P.; Jen, K.-K. Microstructure evolution induced by inoculants during the selective laser melting of IN718. *Addit. Manuf.* **2018**, *21*, 465–471. [CrossRef]
13. Kakehi, K.; Banoth, S.; Kuo, Y.-L.; Hayashi, S. Effect of yttrium addition on creep properties of a Ni-base superalloy built up by selective laser melting. *Scr. Mater.* **2020**, *183*, 71–74. [CrossRef]
14. Poyraz, Ö.; Kuşhan, M.C. Residual Stress-induced Distortions in Laser Powder Bed Additive Manufacturing of Nickel-based Superalloys. *Stroj. Vestn. J. Mech. Eng.* **2019**, *65*, 343–350. [CrossRef]
15. Diepold, B.; Vorlaufer, N.; Neumeier, S.; Gartner, T.; Göken, M. Optimization of the heat treatment of additively manufactured Ni-base superalloy IN718. *Int. J. Miner. Metall. Mater.* **2020**, *27*, 640–648. [CrossRef]
16. Ho, I.-T.; Hsu, T.-H.; Chang, Y.-J.; Li, C.-W.; Chang, K.-C.; Tin, S.; Kakehi, K.; Yeh, A.-C. Effects of CoAl2O4 inoculants on microstructure and mechanical properties of IN718 processed by selective laser melting. *Addit. Manuf.* **2020**, *35*, 101328. [CrossRef]
17. Hsu, T.-H.; Chang, K.-C.; Chang, Y.-J.; Ho, I.-T.; Tin, S.; Li, C.-W.; Kakehi, K.; Chen, C.-P.; Jen, K.-K.; Hsieh, H.-Y.; et al. Effect of Carbide Inoculants Additions in IN718 Fabricated by Selective Laser Melting Process. In *Superalloy 2020*; Tin, S., Hardy, M., Clews, J., Cormier, J., Feng, Q., Marcin, J., O'Brien, C., Suzuki, A., Eds.; Springer: Cham, Switzerland, 2020; pp. 982–989. [CrossRef]
18. Kuo, Y.-L.; Horikawa, S.; Kakehi, K. The effect of interdendritic δ phase on the mechanical properties of Alloy 718 built up by additive manufacturing. *Mater. Des.* **2017**, *116*, 411–418. [CrossRef]
19. Gallmeyer, T.G.; Moorthy, S.; Kappes, B.B.; Mills, M.J.; Amin-Ahmadi, B.; Stebner, A.P. Knowledge of process-structure-property relationships to engineer better heat treatments for laser powder bed fusion additive manufactured Inconel 718. *Addit. Manuf.* **2020**, *31*, 100977. [CrossRef]
20. Dinda, G.P.; Dasgupta, A.K.; Mazumder, J. Texture control during laser deposition of nickel-based superalloy. *Scr. Mater.* **2012**, *67*, 503–506. [CrossRef]
21. Baufeld, B. Mechanical Properties of INCONEL 718 Parts Manufactured by Shaped Metal Deposition (SMD). *J. Mater. Eng. Perform.* **2012**, *21*, 1416–1421. [CrossRef]
22. Qi, H.; Azer, M.; Ritter, A. Studies of Standard Heat Treatment Effects on Microstructure and Mechanical Properties of Laser Net Shape Manufactured INCONEL 718. *Metall. Mater. Trans. A* **2009**, *40*, 2410–2422. [CrossRef]
23. Sui, S.; Tan, H.; Chen, J.; Zhong, C.; Li, Z.; Fan, W.; Gasser, A.; Huang, W. The influence of Laves phases on the room temperature tensile properties of Inconel 718 fabricated by powder feeding laser additive manufacturing. *Acta Mater.* **2019**, *164*, 413–427. [CrossRef]

24. Sames, W. Additive Manufacturing of Inconel 718 Using Electron Beam Melting: Processing, Post-Processing, & Mechanical Properties. Ph.D. Thesis, Texas Agricultural and Mechanical University, College Station, TX, USA, 2015.
25. Tofail, S.A.M.; Koumoulos, E.P.; Bandyopadhyay, A.; Bose, S.; O'Donoghue, L.; Charitidis, C. Additive manufacturing: Scientific and technological challenges, market uptake and opportunities. *Mater. Today* **2018**, *21*, 22–37. [CrossRef]
26. Barroqueiro, B.; Andrade-Campos, A.; Valente, R.A.F.; Neto, V. Metal additive manufacturing cycle in aerospace industry: A comprehensive review. *J. Manuf. Mater. Process.* **2019**, *3*, 52. [CrossRef]
27. Gokuldoss, P.K.; Kolla, S.; Eckert, J. Additive Manufacturing Processes: Selective Laser Melting, Electron Beam Melting and Binder Jetting—Selection Guidelines. *Materials* **2017**, *10*, 672. [CrossRef] [PubMed]
28. Wooldridge, M.; Wangenheim, C.; Herberg, W.; Wettmarshausen, T. Applications of Metal Additive Manufacturing in the Oil and Gas Industry. In Proceedings of the Offshore Technology Conference, Houston, TX, USA, 4–7 May 2020. [CrossRef]
29. Kim, Y.-K.; Choe, J.; Lee, K.-A. Selective laser melted equiatomic CoCrFeMnNi high-entropy alloy: Microstructure, anisotropic mechanical response, and multiple strengthening mechanism. *J. Alloys Compd.* **2019**, *805*, 680–691. [CrossRef]
30. Lin, W.-C.; Chang, Y.-J.; Hsu, T.-H.; Gorsse, S.; Sun, F.; Furuhara, T.; Yeh, A.-C. Microstructure and tensile property of a precipitation strengthened high entropy alloy processed by selective laser melting and post heat treatment. *Addit. Manuf.* **2020**, *36*, 101601. [CrossRef]
31. AlMangour, B.; Kim, Y.-K.; Grzesiak, D.; Lee, K.-A. Novel TiB2-reinforced 316L stainless steel nanocomposites with excellent room- and high-temperature yield strength developed by additive manufacturing. *Compos. Part B Eng.* **2019**, *156*, 51–63. [CrossRef]
32. Mukherjee, T.; Zhang, W.; DebRoy, T. An improved prediction of residual stresses and distortion in additive manufacturing. *Comput. Mater. Sci.* **2017**, *126*, 360–372. [CrossRef]
33. Mukherjee, T.; Manvatkar, V.; De, A.; DebRoy, T. Mitigation of thermal distortion during additive manufacturing. *Scr. Mater.* **2017**, *127*, 79–83. [CrossRef]
34. Lu, Y.; Wu, S.; Gan, Y.; Huang, T.; Yang, C.; Junjie, L.; Lin, J. Study on the microstructure, mechanical property and residual stress of SLM Inconel-718 alloy manufactured by differing island scanning strategy. *Opt. Laser Technol.* **2015**, *75*, 197–206. [CrossRef]
35. Han, Q.; Gu, Y.; Setchi, R.; Lacan, F.; Johnston, R.; Evans, S.L.; Yang, S. Additive manufacturing of high-strength crack-free Ni-based Hastelloy X superalloy. *Addit. Manuf.* **2019**, *30*, 100919. [CrossRef]
36. Beaubois, V.; Huez, J.; Coste, S.; Brucelle, O.; Lacaze, J. Short term precipitation kinetics of delta phase in strain free Inconel* 718 alloy. *Mater. Sci. Technol.* **2004**, *20*, 1019–1026. [CrossRef]
37. *ASTM E8/E8M-21 Standard Test Methods for Tension Testing of Metallic Materials*; ASTM International: West Conshohocken, PA, USA, 2016. [CrossRef]
38. Schneider, C.A.; Rasband, W.S.; Eliceiri, K.W. NIH Image to ImageJ: 25 years of image analysis. *Nat. Methods* **2012**, *9*, 671–675. [CrossRef]
39. Moussa, C.; Bernacki, M.; Besnard, R.; Bozzolo, N. Statistical analysis of dislocations and dislocation boundaries from EBSD data. *Ultramicroscopy* **2017**, *179*, 63–72. [CrossRef] [PubMed]
40. Nye, J.F. Some geometrical relations in dislocated crystals. *Acta Metall.* **1953**, *1*, 153–162. [CrossRef]
41. Konijnenberg, P.J.; Zaefferer, S.; Raabe, D. Assessment of geometrically necessary dislocation levels derived by 3D EBSD. *Acta Mater.* **2015**, *99*, 402–414. [CrossRef]
42. Muránsky, O.; Balogh, L.; Tran, M.; Hamelin, C.J.; Park, J.S.; Daymond, M.R. On the measurement of dislocations and dislocation substructures using EBSD and HRSD techniques. *Acta Mater.* **2019**, *175*, 297–313. [CrossRef]
43. Kamaya, M. Assessment of local deformation using EBSD: Quantification of accuracy of measurement and definition of local gradient. *Ultramicroscopy* **2011**, *111*, 1189–1199. [CrossRef] [PubMed]
44. Abbaschian, R.; Abbaschian, L.; Reed-Hill, R.E. *Physical Metallurgy Principles*, 4th ed.; SI vesrion; CENGAGE Learning: Boston, MA, USA, 2010; ISBN 978-0495438519.
45. Gu, D.; Ma, C.; Xia, M.; Dai, D.; Shi, Q. A Multiscale Understanding of the Thermodynamic and Kinetic Mechanisms of Laser Additive Manufacturing. *Engineering* **2017**, *3*, 675–684. [CrossRef]
46. AlMangour, B.; Grzesiak, D.; Borkar, T.; Yang, J.-M. Densification behavior, microstructural evolution, and mechanical properties of TiC/316L stainless steel nanocomposites fabricated by selective laser melting. *Mater. Des.* **2018**, *138*, 119–128. [CrossRef]
47. Kou, S. Basic Solidification Concepts. In *Welding Metallurgy*; John Wiley & Sons: Hoboken, NJ, USA, 2002; pp. 143–169. [CrossRef]
48. Smith, T.R.; Sugar, J.D.; San Marchi, C.; Schoenung, J.M. Strengthening mechanisms in directed energy deposited austenitic stainless steel. *Acta Mater.* **2019**, *164*, 728–740. [CrossRef]
49. Wang, G.; Ouyang, H.; Fan, C.; Guo, Q.; Li, Z.; Yan, W.; Li, Z. The origin of high-density dislocations in additively manufactured metals. *Mater. Res. Lett.* **2020**, *8*, 283–290. [CrossRef]
50. Birnbaum, A.J.; Steuben, J.C.; Barrick, E.J.; Iliopoulos, A.P.; Michopoulos, J.G. Intrinsic strain aging, Σ3 boundaries, and origins of cellular substructure in additively manufactured 316L. *Addit. Manuf.* **2019**, *29*, 100784. [CrossRef]
51. Ci, S.; Liang, J.; Li, J.; Wang, H.; Zhou, Y.; Sun, X.; Zhang, H.; Ding, Y.; Zhou, X. Prediction of Primary Dendrite Arm Spacing in Pulsed Laser Surface Melted Single Crystal Superalloy. *Acta Metall. Sin. (Engl. Lett.)* **2020**, *34*, 485–494. [CrossRef]
52. Manikandan, S.G.K.; Sivakumar, D.; Rao, K.P.; Kamaraj, M. Laves phase in alloy 718 fusion zone—Microscopic and calorimetric studies. *Mater. Charact.* **2015**, *100*, 192–206. [CrossRef]
53. Cuppari, M.; Santos, S. Physical Properties of the NbC Carbide. *Metals* **2016**, *6*, 250. [CrossRef]

54. Han, Y.; Deb, P.; Chaturvedi, M.C. Coarsening behaviour of γ''- and γ'-particles in Inconel alloy 718. *Met. Sci.* **1982**, *16*, 555–562. [CrossRef]
55. Kleemola, H.J.; Nieminen, M.A. On the strain-hardening parameters of metals. *Metall. Trans.* **1974**, *5*, 1863–1866. [CrossRef]
56. Meyers, M.A.; Chawla, K.K. *Mechanical Behavior of Materials*, 2nd ed.; Cambridge University Press: Cambridge, UK, 2008. [CrossRef]
57. Sanaty-Zadeh, A. Comparison between current models for the strength of particulate-reinforced metal matrix nanocomposites with emphasis on consideration of Hall–Petch effect. *Mater. Sci. Eng. A* **2012**, *531*, 112–118. [CrossRef]
58. Kozar, R.W.; Suzuki, A.; Milligan, W.W.; Schirra, J.J.; Savage, M.F.; Pollock, T.M. Strengthening Mechanisms in Polycrystalline Multimodal Nickel-Base Superalloys. *Metall. Mater. Trans. A* **2009**, *40*, 1588–1603. [CrossRef]
59. Mughrabi, H. A two-parameter description of heterogeneous dislocation distributions in deformed metal crystals. *Mater. Sci. Eng.* **1987**, *85*, 15–31. [CrossRef]
60. Hong, Y.; Zhou, C.; Zheng, Y.; Zhang, L.; Zheng, J. The cellular boundary with high density of dislocations governed the strengthening mechanism in selective laser melted 316L stainless steel. *Mater. Sci. Eng. A* **2021**, *799*, 140279. [CrossRef]
61. Cheng, Y.; Xiao, Z.; Zhu, H.; Zeng, X.; Wang, G. Influence of substrate characteristics on residual stress of SLMed Inconel 718. *Rapid Prototyp. J.* **2019**, *25*, 792–799. [CrossRef]
62. Reed, R.C. The physical metallurgy of nickel and its alloys. In *The Superalloys: Fundamentals and Applications*; Cambridge University Press: Cambridge, UK, 2006; pp. 33–120. [CrossRef]
63. Chaturvedi, M.C.; Han, Y. Strengthening mechanisms in Inconel 718 superalloy. *Met. Sci.* **1983**, *17*, 145–149. [CrossRef]
64. AMS F Corrosion Heat Resistant Alloys Committee. *Nickel Alloy, Corrosion and Heat-Resistant, Bars, Forgings, and Rings 52.5Ni-19Cr-3.0Mo-5.1Cb (Nb)-0.90Ti-0.50Al-18Fe Consumable Electrode or Vacuum Induction Melted 1775 °F (968 °C) Solution and Precipitation Heat Treated (SAE AMS 5663)*; SAE International: Warrendale, PA, USA, 2016. [CrossRef]